Dark/bright band of a melting layer detected by coherent Doppler lidar and micro rain radar

TIANWEN WEI,[1] HAIYUN XIA,[1,2,3,4,*] KENAN WU,[1,2] YUANJIAN YANG,[1,2] QI LIU,[1] AND WEIDONG DING[5]

[1] *School of Earth and Space Science, University of Science and Technology of China, Hefei 230026, China*
[2] *School of Atmospheric Physics, Nanjing University of Information Science and Technology, Nanjing 210044, China*
[3] *Hefei National Laboratory for Physical Sciences at the Microscale, Hefei 230026, China*
[4] *Institude of Software, Chinese Academy of Science, Beijing 100190, China*
[5] *Anhui Meteorological Observatory, Hefei 230031, China*
[*] *hsia@ustc.edu.cn*

Abstract: Observation of a melting layer using a 1.55 µm coherent Doppler lidar (CDL) is first presented during a stratiform precipitation event. Simultaneous radar measurements are also performed by co-located 1.24 cm micro rain radar (MRR) and 10.6 cm Doppler weather radar (DWR). As a well-known bright band in radar reflectivity appears during precipitation, an interesting dark band about 160 m below that in lidar backscattering is observed. Due to the absorption effect, the backscattering from raindrops at 1.55 µm is found much weaker than that at short wavelengths usually used in direct detection lidars. However, the CDL provides additional Doppler information which is helpful for melting layer identification. For example, a spectrum bright band with broadened width and sign conversion of skewness is detected in this case. After a deep analysis of the power spectra, the aerosol and precipitation components are separated. The fall speed of hydrometeors given by CDL is found smaller than that of MRR, with the differences of approximately 0.5 m/s and 1.5 m/s for the snow and rainfall, respectively. To illustrate the influence of absorption effect, simulations of the backscatter coefficient and extinction coefficient of aerosol and rainfall are also performed at the wavelength range of 0.3 ~ 2.2 µm using the Mie theory.

1. Introduction

It has been recognized that, in middle to high latitudes, most rainfall events at the surface originate from snow [1]. The transition region from snowflakes to raindrops below the 0°C isotherm is called melting layer (ML), in stratiform precipitation [2]. It can influence the surrounding environment [3] and the dynamics of precipitation systems [4,5], by latent heat exchange. Microphysical observations of ML can be performed using occasional aircraft-based penetrations. Continuous detections are provided by ground-based remote sensing instruments, such as radars and lidars. The wavelength-dependent scattering characteristics determine the manifestation of ML and thus the interpretation of the real microphysical process [6,7].

Weather radars have been widely deployed for precipitation monitor and forecast. A commonly known feature during the melting of snowflakes is the enhanced radar reflectivity, referred to as radar bright band. Two main reasons are reposeful for this phenomenon. Firstly, as the melting begins, the water-coated snowflakes increase the radar reflectivity, because the dielectric constant of water is approximately 5 times that of ice [8]. Secondly, as the snowflakes collapse into raindrops, the faster speed of raindrops causes reduced volume number concentration and thus a decrease in reflectivity [9]. The presence of a bright band also depends on the radar wavelength. At short millimeter wavelengths, a bright band is typically absent, for example, a radar dark band was reported even at 3.2 mm (94 GHz), due to non-Rayleigh scattering effects [10,11].

Lidars generally work in clear conditions, as it's hard for the laser to penetrate thick clouds occurring in most precipitations. However, from serendipitous lidar observations, a lidar dark band has been reported at a height not far below the radar bright band peak, which is associated with the structural collapse and accumulation of melted snowflakes and their transition to spherical drops. Sassen firstly studied this phenomenon comprehensively and named it as lidar dark band [12]. The conceptual microphysical/scattering model on the interpretation of dark band was also elaborated and confirmed [9,10].

In previous studies, the lidars used are limited to relatively short wavelengths, including three-wavelength Raman lidar (1064 nm, 532 nm, 355 nm, [9,13]), 523 nm micro-pulse lidar [10], and 905 nm ceilometer [14], where backscattering intensity (sometimes plus depolarization ratio) is provided. The detection of melting layer using a CDL with longer wavelengths has not been reported yet. Velocity information in the light scattering regime provided by Doppler lidar will be helpful for the interpretation of melting microphysical processes and in separating the aerosol contribution from the total backscattering.

Coherent detection provides the capability to measure range-resolved backscattering intensity and velocity using the Doppler effect [15]. In atmospheric remote sensing, pulsed lasers are generally adopted to obtain range information based on time of flight [16]. For hard target detection, modulation technologies are often applied to achieve higher resolution. For example, amplitude-modulated continuous-wave lidar [17], frequency-modulated continuous-wave lidar [18], multi-tone continuous-wave lidar [19] and other methods [20].

In this study, an all-fiber pulsed CDL operating at 1.55 μm is applied for melting layer detection. The datasets from a nearby MRR and a DWR are also used for comparison. A 10-hour stratiform precipitation event over the Hefei region on 26–27 December 2020 is reported. The melting process is verified in the Doppler domain in the optical wavelength region. The differences in the manifestation of melting layer between 1.55 μm Doppler lidar and that with shorter-wavelengths used in previous researches are explained.

2.　Instruments and datasets

The datasets from three remote sensing instruments are used in the study. The CDL and MRR are installed on the campus of the University of Science and Technology of China (USTC) (31.83°N, 117.25°E). The DWR is located 3.5 km away in the northwest. The key parameters are summarized in Table 1. Besides, A ground-based optical disdrometer (second-generation particle size and velocity, Parsivel-2 [21]) and a Davis weather station (wireless vantage pro2 plus) are also deployed for comparative measurements within 15 m away from the CDL.

Table 1. Key parameters of CDL, MRR, and DWR

Parameter	CDL	MRR	DWR
Wavelength	1.55 μm	1.24 cm	10.6 cm
Transmitter type	Pulsed (600 ns)	FMCW	Pulsed (1.54 μs)
Transmitter power	3 W (mean)	50 mW (mean)	650 kW (peak)
Pulse repetition rate	10 kHz	——	318 ~ 1300 Hz
Time resolution	1 s	10 ~ 60 s	0.1 s
Range gate length	30 m	70 m	1 km
Maximum detection range	15 km	2.1 km	230 km
Minimum detection range	120 m	140 m	2 km
Antenna diameter	10 cm	60 cm	8.54 m
Beam full divergence	46 μrad	1.5°	0.99°

The eye-safe wavelength of 1.55 µm is often adopted in commercially available coherent Doppler wind lidars, due to its compact fiber laser system and narrow linewidth which is required for coherent detection. Besides, compared to short wavelengths, it suffers smaller influences from atmospheric turbulence and background solar radiation, which helps to achieve all-day operation. The all-fiber CDL used in the experiment is designed for long-range wind and aerosol detection. It has been applied for researches on the atmospheric boundary layer height [22,23], gravity waves [24], turbulence [25,26], and precipitation [27,28]. During this experiment, the CDL operates at velocity-azimuth display (VAD) scan mode at a fixed elevation angle of 65° with a scan period of 2 minutes. The detailed information about the system is presented in previous works [29,30].

The K-band Micro Rain Radar is a vertically pointing frequency modulated continuous wave (FMCW) radar (MRR-2, METEK Germany). It operates with microwave at a frequency of 24.23 GHz with modulation of 0.5–15 MHz according to the height resolution. The wavelength is selected after trade-offs between the sensitivity to small raindrops and the rain attenuation effect [31]. In this study, the temporal and spatial resolutions of the MRR are set as 1 min and 70 m, respectively.

The 10.6 cm S-band Doppler weather radar deployed in Hefei is the first one of China's New Generation Weather Radar System (CINRAD), typed as CINRAD/SA developed based on the WSR-88D technology [32]. It was installed on the roof of a tower with a height of 116.5 m. During precipitation, the radar works in the volume cover pattern (VCP) performing several low-elevation-angle scans within 6 minutes.

3. Results and analysis

Although there exist limitations for lidars to operate in precipitation environments, interesting phenomena were often captured during long-term observations. On December 26–27, 2020, the Hefei region was affected by a stratiform precipitation system. The ground-level Parsivel-2 recorded light rainfall with a maximum rate of 1.5 mm/h and accumulated rainfall of 2.6 mm. 24-hours continuous observation results of the CDL are shown in Fig. 1(a-c).

As shown in Fig. 1(a), the attenuated backscatter coefficient of CDL is calculated from the wideband carrier-to-noise ratio (CNR) after corrections of range, focus function, and a constant factor. The focus function is retrieved from horizontal scanning results by assuming homogeneous aerosol distribution [33]. The constant factor containing all technical system parameters is derived by the integration of the backscattered signal over the optically thick, non-drizzling stratocumulus that can totally attenuate the laser [34,35]. This correction method is valid during rain-free conditions. When the telescope is covered by raindrops, the received signal intensity will suffer an additional significant reduction due to strong water absorption and coupling efficiency loss, which also becomes one of the limitations on CDL's detection ability in precipitation environments. Compared to direct detection lidars, the requirement of single-mode operation for coherent detection results in extreme sensitivity to the wavefront distortion caused by liquid water remaining on the telescope lens [28]. Accurate correction to the coupling loss is almost impossible, but it won't affect the shape of the derived vertical profiles of Doppler-shifted spectra and the following deep analysis.

Figure 1(b-c) show the spectrum width and skewness, both of which have been applied to identify rainfall event in previous works [25,27]. Although the spectrum width may also be broadened by turbulence and wind shear, the precipitation associated with faster fall speed may be the most important contributor and shows special characteristics. Similarly, the skewness will depart from zero if a rainfall signal exists. Compared to the spectrum width, the skewness is more sensitive in identifying the rainfall but also requires higher CNR.

Lidar signals with attenuated backscatter coefficient approaching 10^{-4} $m^{-1}sr^{-1}$ and narrow spectrum width come from mixed-phase stratiform clouds. Below the clouds, falling ice crystals
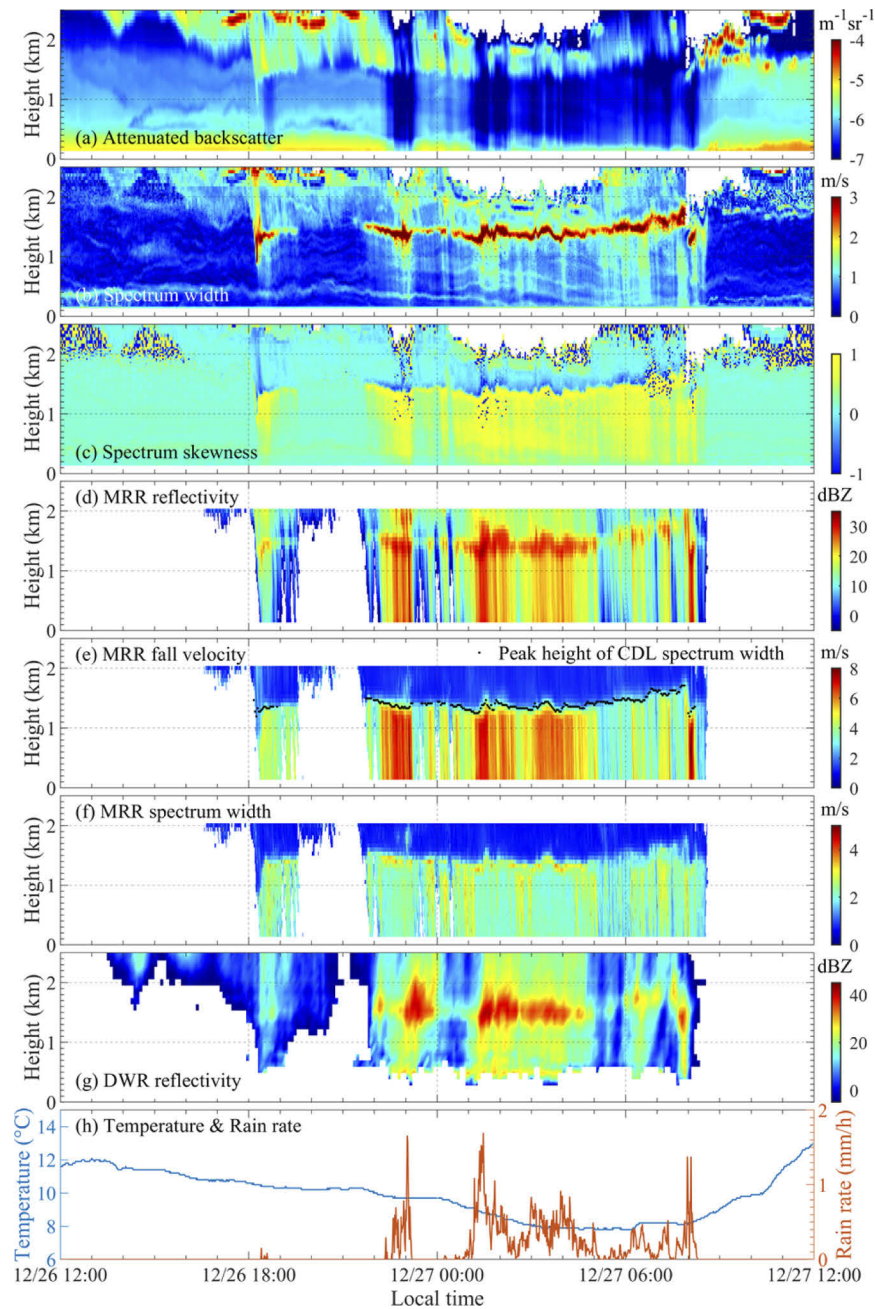
Fig. 1. Continuous observation results of CDL, MRR, and DWR during a stratiform precipitation event on December 26–27, 2020. (a) The attenuated backscatter coefficient, (b) Doppler spectrum width, and (c) spectrum skewness of CDL. (d) The radar reflectivity, (e) fall speed, and (f) spectrum width of MRR. (g) The radar reflectivity of DWR. (h) Temperature and rain rate on the ground level.

are observed with relatively high signal intensity and slightly broadened spectrum width. The clouds and falling hydrometeors can be easily distinguished according to their spectrum width. From 18:00 December 26 to 08:00 December 27, at the height where the hydrometeor signal decreases sharply, a layer with greatly broadened spectrum width and sign conversion of spectrum skewness is seen clearly. Below this layer, the positive skewness reveals the presence of rainfall signal [28]. This layer is therefore inferred as a melting layer by the CDL. Besides, before 18:00 December 26, ice virga is found evaporating due to sub-saturation before reaching the melting level.

Evidence of a melting layer is verified at the height of about 1.5 km by the bright band in radar reflectivity, and the abrupt change in radar fall speed and spectrum width in the measurements of MRR, as shown in Fig. 1(d-f). The fall speed of snowflakes usually does not exceed 2 m/s and has less dependence on the shape [36]. While the fall speed of raindrops varies largely with the size. The terminal speed of a raindrop with a diameter of 0.5 mm can reach 2 m/s [37]. The ice virga signal observed by CDL is also verified by MRR measurements. At 18:20 December 26, the signal with broadened width extends from the height of 2.5 km to about 0.8 km. These are probably small hail with faster fall speed than snowflakes and require more time to melt. The superposition of hail signal and cloud signal also broadens the spectrum.

Measurement results of the DWR give a broad view of the stratiform precipitation process. Figure 2 shows a typical example of the radar reflectivity obtained at 6° elevation angle scanning. The location of USTC is marked on the figure with a pentagram. A red ring (i.e., bright band) can be seen clearly at the radial distance of about 14 km. Regarding the elevation angle, the height of the melting layer is calculated to be 1.5 km, which is consistent with that obtained from the CDL and MRR. The time-height plot of the reflectivity of DWR is also shown in Fig. 1(g). It is calculated from the scanning results at the elevation angle of 6° and azimuth angles along the wind direction. Due to the large difference in the sensing volume with the other two instruments, it is only used as a reference.
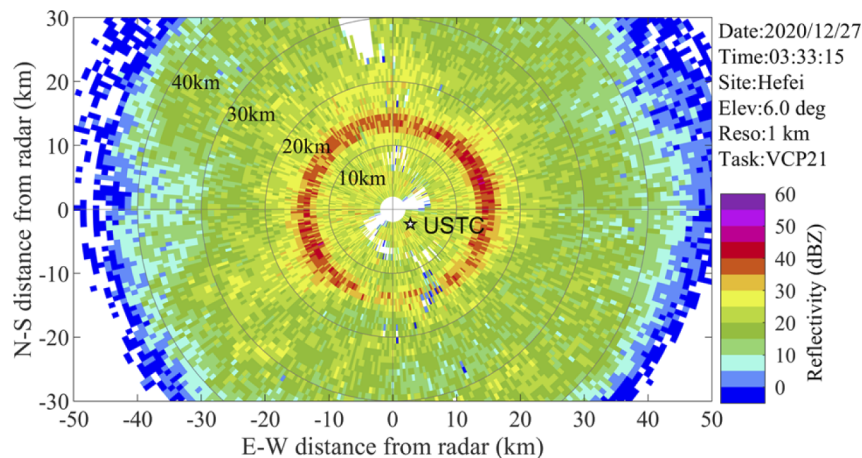

Fig. 2. Level-II reflectivity from Hefei S-band DWR observed at 6° elevation angle at 03:30 local time. The red ring (i.e., bright band) between the radial distance of about 14 km indicates the melting layer.

Compared with previous works using short-wavelength lidars [9,10,14], the so-called lidar dark band at 1.55 μm seems not clear at the melting layer. Because the backscattering from raindrops is much weaker than that from snowflakes, and the signal below the melting layer is dominated by the aerosols. This phenomenon is caused by the absorption effect of large raindrops, which will be discussed later in detail. Interestingly, the spectrum width and skewness of CDL show

more obvious features at the melting layer. The melting layer height determined by the position of maximum spectrum width is plotted in Fig. 1(e). The time-varying trend is almost the same as the MRR measurements. Some detailed features, such as lower melting layer height at 18:20 December 26 and 08:20 December 27, also show good consistency.

Figure 3 illustrates the CDL and MRR data expressed in terms of 10-minute averaged Doppler spectra and corresponding vertical profiles over the time interval 02:30-02:40 on December 27. Note that the Doppler power spectrum of CDL shown in panel (d) is an equivalent vertical detection spectrum derived from the radial spectra by compensating the Doppler effect of the horizontal wind. Besides, the broaden effect of the temporal window is also removed through an iterative deconvolution processing to show better contrast [28]. Then the backscatter coefficient and vertical velocity profiles of aerosol signal and precipitation signal are separated and retrieved using the two-peak fitting method [27].
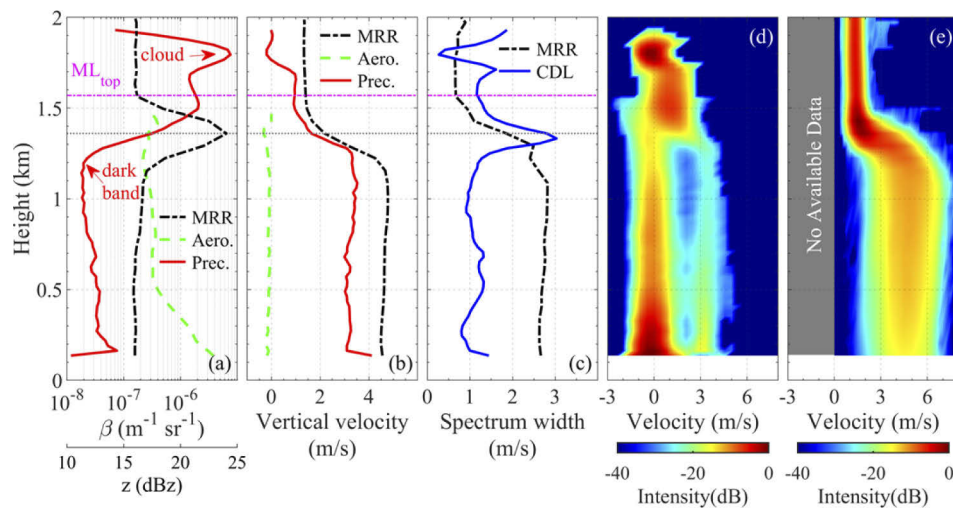
Fig. 3. Typical observation results of the CDL and MRR averaged over the time interval 02:30–02:40 December 27. (a) The attenuated backscatter coefficient β of aerosol signal (green dashed line) and precipitation signal (red line) retrieval from CDL, and the radar reflectivity z (black dashed line) from MRR. (b) The same as (a) but for vertical velocity. (c) Spectrum width obtained from CDL and MRR. (d) Doppler power spectrum of CDL. (e) Doppler power spectrum of MRR. The intensity of (d) and (e) are normalized by the maximum. The ML top is estimated as the height where the slope of the reflectivity profile changes. The mean rain rate during the 10-minutes interval is 0.12 mm/h.

As shown in Fig. 3(a), the vertical profile of the radar reflectivity of MRR reveals the presence of the radar bright band with a peak at approximately 1.36 km. The lidar attenuated backscatter coefficient of precipitation signal shows a dark band at about 1.2 km, about 160 m below the radar bright band, which is consistent with previous reports [9,10]. Both the structural collapse induced size decrease, and the reduced volume number concentration due to the faster fall speed of raindrops contribute to the decrease of precipitation backscattering. Besides, the growth of rain droplets through the collision-coalescence process can also reduce the lidar signal, as the D^2 dependence in geometric scattering is weak than the volume dependence of D^3, which is opposite to the situation of radar where the D^6 relation holds. However, just below the dark band, the signal enhancement associated with the spherical particle backscattering mechanisms [10] is very weak. The strong absorption effect at 1.55 μm is probably the reason. Two lidar bright bands are also observed at heights of 1.5 km and 1.8 km, which are associated with the combined contributions of the increasing snowflake/cloud backscattering with height and the pronounced

attenuation of the laser beam in the snowfall/cloud region, respectively. It's noted that the large fluctuation of precipitation signal below the height of 300 m is due to the influence of the nearby strong aerosol signal.

Figure 3(b) shows the profiles of mean vertical velocities measured by CDL and MRR. As expected, the vertical wind speed represented by aerosol motion is close to zero. The fall speed of hydrometeors given by MRR is always larger than that of the CDL, with the differences of approximately 0.5 m/s and 1.5 m/s for the snow and rain, respectively. This is due to that MRR is more sensitive to large particles governed by D^6 power law under Rayleigh scattering, while geometric optics with approximate dependence of D^2 is valid for CDL. Both speeds show a steady increase descending through the melting layer.

Figure 3(c) gives the profiles of spectrum width derived from the Doppler power spectrum of CDL and MRR. Similar to the mean fall speed, the spectrum width increases as passing the transition zone, due to wider speed distribution for raindrops. In this case, the spectrum width of CDL shows a maximum at the height just several meters below the radar reflectivity peak. The decrease of spectrum width below this layer is because the signal is dominated by weak-broaden aerosols. As the MRR is unable to detect aerosol backscatter, its spectrum width keeps.

Figure 4 gives typical examples measured over 02:30–02:40 December 27, to better illustrate the contribution of precipitation particles and aerosol scattering to the Doppler spectra of CDL and the influence on the derived spectrum width and spectrum skewness. As shown in Fig. 4(a), the Doppler spectrum of the snow signal is almost symmetrical, due to the weak dependency of velocity on size. Therefore, slightly broadened spectrum width and skewness approaching zero are observed. Then as the snow melts, its size decreases due to structural collapse, causing decreased backscattering intensity. Meanwhile, the aerosol backscattering increases as the height decreases. In Fig. 4(b), similar intensities are reached, resulting in a wide spectrum width and a sign conversion of skewness (see also Fig. 1(c)). Next, the Doppler spectrum is dominated by aerosol signal, showing a decrease in the value of spectrum width and a positive skewness.
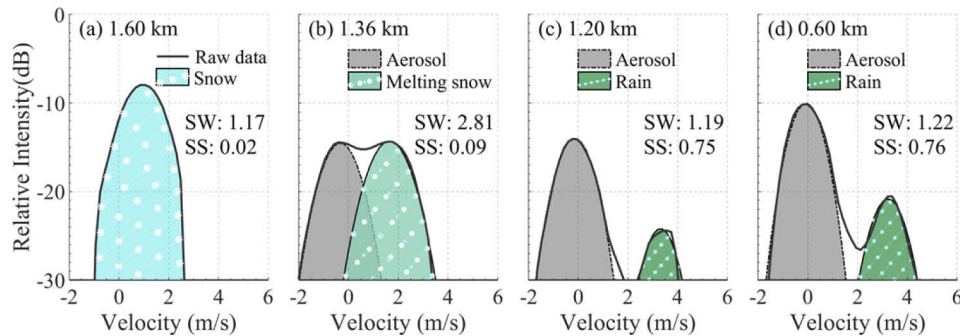

Fig. 4. Typical examples illustrating the contribution of hydrometeor and aerosol scattering to the Doppler spectra of CDL. The data is the same as Fig. 3(d), where the maximum spectrum width locates at 1.36 km and the minimum dark band locates at 1.2 km. The values of spectrum width (SW) and spectrum skewness (SS) are also given.

As expressed in Fig. 4, the characteristics of spectrum width and skewness are affected by the intensity relation between the aerosol and precipitation signal, which depends on the height of the melting layer, the vertical profile of aerosol concentration, and the wavelength of the probing laser. Figure 5 simulates the backscatter coefficient and extinction coefficient of aerosol, rainfall using the following integration

$$g_i(\lambda, \tilde{m}) = \int_{r_{\min}}^{r_{\max}} \pi r^2 Q_i(2\pi r / \lambda, \tilde{m}) N(r) \mathrm{d}r \qquad (1)$$

Where $g_{i=\beta,\sigma}$ represent the backscatter coefficient β and extinction coefficient σ. $Q_{i=\beta,\sigma}$ represent the differential backscatter efficiency and extinction efficiency, calculated using the Mie theory here [38], under the assumption of spheric particles. $N(r)$ is the particle number concentration and r is the radius.
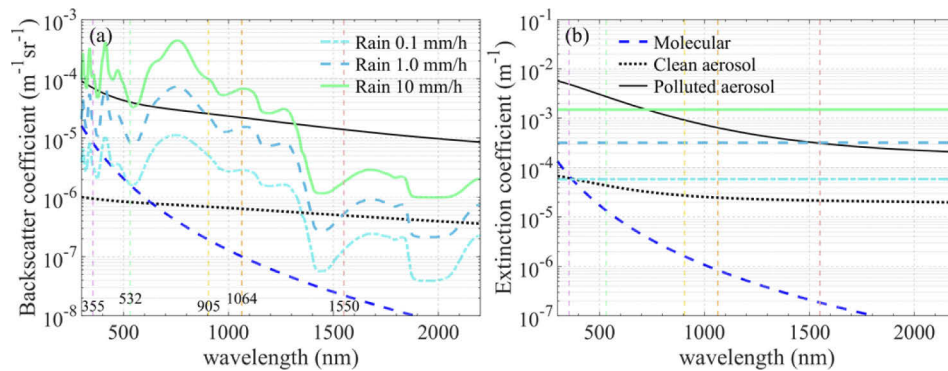
Fig. 5. Simulated backscatter coefficients (a) and extinction coefficients (b) of molecular, clean aerosol, polluted aerosol, and rainfall with three different rates using the Mie scattering theory. The wavelengths of 355 nm, 532 nm, 905 nm, 1064 nm, and 1550 nm are also labeled.

The exponential M-P raindrop size distribution [39] is used in the calculation of rainfall backscattering. But this model generally tends to overestimate the smallest drops [40] which the lidar is very sensitive to [28]. Therefore, a lower limit $r_{\min}$ in the integration is set at 0.15 mm corresponding to a fall speed of 1 m/s. The complex refractive index of liquid water is given by [41].

Two aerosol types are calculated, based on the clean continental and polluted continental type in the CALIPSO aerosol model [42]. The volume concentrations of the fine/coarse mode are set as 5/20 and 400/200 $\mu m^3 cm^{-3}$, respectively. The refractive indexes are set as 1.40–0.0035i and 1.50–0.01i without wavelength dependency, respectively [43]. In addition, the molecular scatter at ground level is given according to the standard atmospheric model.

Figure 5(a) explains the reason why the backscattering of rain is much weak than that of aerosol at the wavelength of 1.55 μm in the present case. The rain backscattering at the other four shorter wavelengths (i.e., 355 nm, 532 nm, 905 nm,1064 nm) is 1~2 order of magnitude larger than that of 1.55 μm. While the difference of aerosol backscattering is small. Thus, the rain backscattering easily dominates the received signal at these short wavelengths. The absorption effect is responsible for this phenomenon. For all wavelengths, the extinction efficiency quickly reaches the limitation of 2 as the raindrop size increases, while the absorption increases with size. The increase in absorption means a decrease in scattering and thus backscattering. Due to more absorption at 1.55 μm, its backscattering is weak. The differential backscattering of multi-wavelength lidars has been used to estimate drizzle drop size [44,45].

The scattering of snowflakes is much complex, depending on the specific shape and orientation. For oriented ice crystals, 2° away from vertical can decrease the measured backscattering intensity by an order of magnitude [35]. In the present case, the backscattering of snowflakes is about 2 orders of magnitude larger than that of the raindrops, and similar to the intensity of ground-level aerosol. The spectrum bright band with sign conversion of skewness is formed at the intersection between the decreased melting snow signal and the increased aerosol signal. In the cases where the aerosol signal is comparable with or weaker than the rain signal below the melting layer, the broadened spectrum width will be maintained until the aerosol signal dominate, due to the wide velocity distribution of raindrops. In other cases, if the melting appears inside the boundary layer with a high aerosol load, for example, pollution conditions, its manifestation on the backscatter

coefficient, spectrum width, and skewness may be unobvious. Deep analysis of the Doppler spectrum is needed, as performed in Fig. 3.

4. Conclusion

In this paper, observations of the melting layer were reported based on the CDL, during a stratiform precipitation event on December 26–27, 2020. The co-located MRR and DWR presented a traditional bright band at the melting layer, while a lidar dark band was observed by the CDL. Besides, a spectrum bright band with broadened width and sign conversion of skewness was also observed.

The differences in backscattering intensity of rainfall between 1.55 um and short wavelengths used in direct detection lidars were explained by a simulation. The influence of the melting layer height and vertical profile of aerosol concentration on the Doppler spectrum of CDL were also discussed. For future work, we plan to add depolarization information that was not available during the present case, and combine multi-wavelength lidars and radars for researches on the microphysics process of melting.

References

1. P. R. Field and A. J. Heymsfield, "Importance of snow to global precipitation," Geophys. Res. Lett. **42**(21), 9512–9520 (2015).
2. F. Fabry and I. Zawadzki, "Long-term radar observations of the melting layer of precipitation and their interpretation," J. Atmos. Sci. **52**(7), 838–851 (1995).
3. J. T. Carlin and A. V. Ryzhkov, "Estimation of melting-layer cooling rate from dual-polarization radar: Spectral bin model simulations," J. Appl. Meteorol. Climatol. **58**(7), 1485–1508 (2019).
4. R. E. Stewart, J. D. Marwitz, J. C. Pace, and R. E. Carbone, "Characteristics through the melting layer of stratiform clouds," J. Atmos. Sci. **41**(22), 3227–3237 (1984).
5. K. K. Szeto, C. A. Lin, and R. E. Stewart, "Mesoscale circulations forced by melting snow. Part I: Basic simulations and dynamics," J. Atmos. Sci. **45**(11), 1629–1641 (1988).
6. H. Li and D. Moisseev, "Two layers of melting ice particles within a single radar bright band: Interpretation and implications," Geophys. Res. Lett. **47**(13), e2020GL087499 (2020).
7. H. Li, J. Tiira, A. von Lerber, and D. Moisseev, "Towards the connection between snow microphysics and melting layer: insights from multifrequency and dual-polarization radar observations during BAECC," Atmos. Chem. Phys. **20**(15), 9547–9562 (2020).
8. S. Evans, "Dielectric properties of ice and snow–a review," J. Glaciol. **5**(42), 773–792 (1965).
9. P. D. Girolamo, D. Summa, M. Cacciani, E. G. Norton, G. Peters, and Y. Dufournet, "Lidar and radar measurements of the melting layer: observations of dark and bright band phenomena," Atmos. Chem. Phys. **12**(9), 4143–4157 (2012).
10. K. Sassen, J. R. Campbell, J. Zhu, P. Kollias, M. Shupe, and C. Williams, "Lidar and triple-wavelength Doppler radar measurements of the melting layer: A revised model for dark- and brightband phenomena," J. Appl. Meteorol. **44**(3), 301–312 (2005).
11. P. Kollias and B. Albrecht, "Why the melting layer radar reflectivity is not bright at 94 GHz," Geophys. Res. Lett. **32**(24), L24818 (2005).
12. K. Sassen and T. Chen, "The lidar dark band: An oddity of the radar bright band analogy," Geophys. Res. Lett. **22**(24), 3505–3508 (1995).
13. Y. Yi, F. Yi, F. C. Liu, Y. P. Zhang, C. M. Yu, and Y. He, "Microphysical process of precipitating hydrometeors from warm-front mid-level stratiform clouds revealed by ground-based lidar observations," Atmos. Chem. Phys. **21**(23), 17649–17664 (2021).
14. A. E. Emory, B. Demoz, K. Vermeesch, and M. Hicks, "Double bright band observations with high-resolution vertically pointing radar, lidar, and profilers," J. Geophys. Res. Atmos. **119**(13), 8201–8211 (2014).
15. T. Fujii and T. Fukuchi, *Laser remote sensing* (CRC press, 2005).
16. Y. Zhang, Y. Wu, and H. Xia, "Spatial resolution enhancement of coherent Doppler wind lidar using differential correlation pair technique," Opt. Lett. **46**(22), 5550–5553 (2021).
17. J. T. Spollard, L. E. Roberts, C. S. Sambridge, K. McKenzie, and D. A. Shaddock, "Mitigation of phase noise and Doppler-induced frequency offsets in coherent random amplitude modulated continuous-wave LiDAR," Opt. Express **29**(6), 9060–9083 (2021).

18. M. U. Piracha, D. Nguyen, I. Ozdur, and P. J. Delfyett, "Simultaneous ranging and velocimetry of fast moving targets using oppositely chirped pulses from a mode-locked laser," Opt. Express **19**(12), 11213–11219 (2011).

19. M. M. Bayer, X. Li, G. N. Guentchev, R. Torun, J. E. Velazco, and O. Boyraz, "Single-shot ranging and velocimetry with a CW lidar far beyond the coherence length of the CW laser," Opt. Express **29**(26), 42343–42354 (2021).

20. D. Onori, F. Scotti, M. Scaffardi, A. Bogoni, and F. Laghezza, "Coherent interferometric dual-frequency laser radar for precise range/doppler measurement," J. Lightwave Technol. **34**(20), 4828–4834 (2016).

21. A. Tokay, D. B. Wolff, and W. A. Petersen, "Evaluation of the new version of the laser-optical disdrometer, OTT parsivel," J. Atmos. Ocean. Technol. **31**(6), 1276–1288 (2014).

22. C. Wang, M. Jia, H. Xia, Y. Wu, T. Wei, X. Shang, C. Yang, X. Xue, and X. Dou, "Relationship analysis of PM2.5 and boundary layer height using an aerosol and turbulence detection lidar," Atmos. Meas. Tech. **12**(6), 3303–3315 (2019).

23. L. Wang, W. Qiang, H. Xia, T. Wei, J. Yuan, and P. Jiang, "Robust Solution for Boundary Layer Height Detections with Coherent Doppler Wind Lidar," Adv. Atmos. Sci. **38**(11), 1920–1928 (2021).

24. M. Jia, J. Yuan, C. Wang, H. Xia, Y. Wu, L. Zhao, T. Wei, J. Wu, L. Wang, and S.-Y. Gu, "Long-lived high-frequency gravity waves in the atmospheric boundary layer: observations and simulations," Atmos. Chem. Phys. **19**(24), 15431–15446 (2019).

25. J. Yuan, H. Xia, T. Wei, L. Wang, B. Yue, and Y. Wu, "Identifying cloud, precipitation, windshear, and turbulence by deep analysis of the power spectrum of coherent Doppler wind lidar," Opt. Express **28**(25), 37406–37418 (2020).

26. J. Yuan, K. Wu, T. Wei, L. Wang, Z. Shu, Y. Yang, and H. Xia, "Cloud Seeding Evidenced by Coherent Doppler Wind Lidar," Remote Sens. **13**(19), 3815 (2021).

27. T. Wei, H. Xia, J. Hu, C. Wang, M. Shangguan, L. Wang, M. Jia, and X. Dou, "Simultaneous wind and rainfall detection by power spectrum analysis using a VAD scanning coherent Doppler lidar," Opt. Express **27**(22), 31235–31245 (2019).

28. T. Wei, H. Xia, B. Yue, Y. Wu, and Q. Liu, "Remote sensing of raindrop size distribution using the coherent Doppler lidar," Opt. Express **29**(11), 17246–17257 (2021).

29. C. Wang, H. Xia, M. Shangguan, Y. Wu, L. Wang, L. Zhao, J. Qiu, and R. Zhang, "1.5 µm polarization coherent lidar incorporating time-division multiplexing," Opt. Express **25**(17), 20663–20674 (2017).

30. T. Wei, H. Xia, Y. Wu, J. Yuan, C. Wang, and X. Dou, "Inversion probability enhancement of all-fiber CDWL by noise modeling and robust fitting," Opt. Express **28**(20), 29662–29675 (2020).

31. G. Peters, B. Fischer, H. Münster, M. Clemens, and A. Wagner, "Profiles of raindrop size distributions as retrieved by microrain radars," J. Appl. Meteorol. **44**(12), 1930–1949 (2005).

32. G. He, G. Li, X. Zou, and P. S. Ray, "Applications of a velocity dealiasing scheme to data from the China new generation weather radar system (CINRAD)," Weather Forecasting **27**(1), 218–230 (2012).

33. P. Pentikäinen, E. J. O'Connor, A. J. Manninen, and P. Ortiz-Amezcua, "Methodology for deriving the telescope focus function and its uncertainty for a heterodyne pulsed Doppler lidar," Atmos. Meas. Tech. **13**(5), 2849–2863 (2020).

34. E. J. O'Connor, A. J. Illingworth, and R. J. Hogan, "A technique for autocalibration of cloud lidar," J. Atmos. Ocean. Technol. **21**(5), 777–786 (2004).

35. C. D. Westbrook, A. J. Illingworth, E. J. O'Connor, and R. J. Hogan, "Doppler lidar measurements of oriented planar ice crystals falling from supercooled and glaciated layer clouds," Q. J. R. Meteorolog. Soc. **136**(646), 260–276 (2010).

36. S. Vázquez-Martín, T. Kuhn, and S. Eliasson, "Shape dependence of snow crystal fall speed," Atmos. Chem. Phys. **21**(10), 7545–7565 (2021).

37. D. Atlas, R. C. Srivastava, and R. S. Sekhon, "Doppler radar characteristics of precipitation at vertical incidence," Rev. Geophys. **11**(1), 1–35 (1973).

38. C. F. Bohren and D. R. Huffman, *Absorption and scattering of light by small particles* (John Wiley & Sons, 2008).

39. J. S. Marshall, "The distribution of raindrops with size," J. meteor. **5**(4), 165–166 (1948).

40. A. Waldvogel, "The N 0 jump of raindrop spectra," J. Atmos. Sci. **31**(4), 1067–1078 (1974).

41. D. J. Segelstein, "The complex refractive index of water," (1981).

42. A. H. Omar, D. M. Winker, M. A. Vaughan, Y. Hu, C. R. Trepte, R. A. Ferrare, K.-P. Lee, C. A. Hostetler, C. Kittaka, and R. R. Rogers, "The CALIPSO automated aerosol classification and lidar ratio selection algorithm," J. Atmos. Ocean. Technol. **26**(10), 1994–2014 (2009).

43. H. Di, Q. Wang, H. Hua, S. Li, Q. Yan, J. Liu, Y. Song, and D. Hua, "Aerosol microphysical particle parameter inversion and error analysis based on remote sensing data," Remote Sens. **10**(11), 1753 (2018).

44. C. D. Westbrook, R. J. Hogan, E. J. O'Connor, and A. J. Illingworth, "Estimating drizzle drop size and precipitation rate using two-colour lidar measurements," Atmos. Meas. Tech. **3**(3), 671–681 (2010).

45. S. Lolli, E. J. Welton, and J. R. Campbell, "Evaluating Light Rain Drop Size Estimates from Multiwavelength Micropulse Lidar Network Profiling," J. Atmos. Ocean. Technol. **30**(12), 2798–2807 (2013).